energies

Article

Heat Transfer Analysis for Combustion under Low-Gradient Conditions in a Small-Scale Industrial Energy Systems

Mieszko Tokarski * and Rafał Buczyński

Department of Fuels Technology, Faculty of Energy and Fuels, AGH University of Kraków, al. Adama Mickiewicza 30, 30-059 Cracow, Poland; rabuczynski@agh.edu.pl
* Correspondence: mtokarski@agh.edu.pl; Tel.: +48-12-617-56-39

Abstract: The issue of maintaining low-gradient combustion in the conditions of high heat extraction has been investigated numerically in this work. The analyses include the application of a convective boundary condition at the wall (with estimated boiling heat transfer coefficient); analysis of the Internal Recirculation Device's impact on combustion products and heat transfer under low-gradient conditions; and comparison of both traditional and low-gradient combustion modes. It was shown that the Internal Recirculation Device material and geometry has a significant impact on the nitrogen oxide (NO_x) formation mechanism, as NO_2 emission becomes predominant and can rise up to several hundreds ppm. What is more, along with decrease in thermal resistance of the IRD, CO emissions also increase rapidly, even achieving over 2000 ppm. Additionally, the convective heat transfer rate decreased by about 25% after switching from traditional to low-gradient combustion, whereas the radiative mechanism increased by ≈40% compared to traditional mode. It should also be mentioned that the low-gradient combustion applied in this work achieved approximately 10% higher efficiency than conventional combustion.

Keywords: CFD; combustion; low-gradient combustion; heat transfer; fire-tube boiler

check for updates

Citation: Tokarski, M.; Buczyński, R. Heat Transfer Analysis for Combustion under Low-Gradient Conditions in a Small-Scale Industrial Energy Systems. *Energies* **2024**, *17*, 186. https://doi.org/10.3390/en17010186

Academic Editor: Mahmoud Bourouis

Received: 20 November 2023
Revised: 18 December 2023
Accepted: 21 December 2023
Published: 28 December 2023

1. Introduction

Since the dawn of time, mankind has used chemical energy stored in biomass or fossil fuels for heating, lighting, or defense, e.g., against wild predators. What all these areas have in common is the method of recovering this energy—combustion—which remains the main method of energy conversion to this day. The use of fossil fuels increased rapidly during the Industrial Revolution, which sought a convenient and efficient way to use the enthalpy of combustion products. At that time, the first fire-tube boilers were designed. Today, fire-tube boilers are a mature, well-known, and widespread technology, successfully used in many industry branches to generate heat and steam for technological processes [1,2].

Fire-tube boilers are supplied with different fuels, from coal powder through biomass to natural gas and heavier hydrocarbons, like diesel [3]. They are characterized by high thermal efficiency (>90%) combined with a simple and compact structure. The construction variant and power output (most often between several to even 30 MW) of such boilers depend on the energy demand and required steam parameters (mostly around 20 bar, saturated or slightly superheated) [4–7].

Pro-environmental legislation from the EU encourages modernization of industry via switching to more efficient and environmentally friendly solutions, allowing for reducing or even for complete elimination of pollutant emissions [7–9]. This trend also touches industrial boilers, in which traditional combustion accompanied by low-NO burners is today's standard. This allows us to meet emission standards and conveniently operate boilers using common fuels like coal powder or natural gas. However, in recent years significant interest has been paid to technologies that enable a clean energy recovery from still abundant fossil fuels. Some researchers have sought for the solution in membrane technology (i.e., oxy-fuel combustion), which could be implemented in fire-tube boilers by completely replacing conventional combustion [9–11], or they have investigated the potential effects of various additives to the fuel [12]. There are also works concerning improvements to the boiler control systems which are especially valuable during dynamic work [5,6,13,14]. Some other researchers, on the other hand, pay attention once again to the so-called Low-Gradient Combustion (LGC) also known as MILD (Moderate or Intense Low-oxygen Dilution), HiTAC (High-Temperature Air Combustion), Highly Preheated Air Combustion (HPAC), Colorless Distributed Combustion (CDC), FLOX (Flameless Oxidation), or FC (Flameless Combustion) [15–20]. This concept comes down to expanding the reaction zone to all the available volumes within the combustion chamber (a more uniformly distributed and diluted reactant) by means of enhanced flue gas recirculation, resulting in a uniform temperature profile with lowered peak temperatures by approximately several hundred Kelvins. This leads to a situation where the flame is no longer visible—hence, the term flameless or colorless [21]. This enables a wider range of stable combustion, lower pollutant emissions, and the ability to combust lean and alternative fuels (e.g., syngas, hydrogen). Low-gradient technology fits into the environmental objectives promoted by the EU and constitutes a clean, convenient, and promising way to use a wide range of fuels along with a waste disposal method. What is more, low-gradient combustion is seen as a very promising technology for efficient pure hydrogen (or hydrogen blends) combustion [15,22,23].

So far, low-gradient combustion has been successfully implemented in many industrial applications, but small-scale boilers (up to approx. 30 MW) using LGC are still absent. The reason for this lies in specific conditions that need to be met to sustain a low-gradient mode: the fuel and oxidizer need to be heated to above self-ignition temperatures (approx. >1200 K) and intensive recirculation of the flue gas is required (or properly distributed inlets of reactants). Both conditions can be fulfilled when the boiler dedicated for LGC is properly designed. This, however, is not a simple task, as heat and mass transfer in low-gradient combustion are significantly different than in well-known conventional combustion. Additionally, the structure of classic fire-tube boilers is not favorable for implementation of low-gradient combustion due to high heat extraction from the combustion chamber (which is immersed in boiling water) and due to the lack of combustion substrate's pre-heating. Excessively high heat extraction is particularly important as it leads to LGC combustion instability or extinction, regardless of the substrates' pre-heating. This issue has been addressed by Xu et al. [24], Wang et al. [19], Luan et al. [25], or more recently by Xu et al. [26] once again. In [24], Xu et al. compared numerically conventional and MILD combustion of methane-air under different heat extractions by altering furnace wall temperature (T_{wall}) boundary conditions from 300 K to 1800 K. According to their analysis, MILD combustion could not be sustained below T_{wall} = 950 K, which confirms that, in this mode, the temperature in the reaction zone must be maintained above the self ignition point. Conventional combustion, however, was successfully realized within the considered temperature range. Analysis performed by Luan et al. [25] showed that increasing heat extraction (depending on oxygen mole fraction) leads to the route MILD $\rightarrow$ unsteady combustion $\rightarrow$ extinction; or through HiTAC $\rightarrow$ conditional MILD $\rightarrow$ MILD (unconditional) $\rightarrow$ unsteady combustion $\rightarrow$ extinction. This effect can be compensated (at least partially) by temperature increase in the substrates (pre-heat). They also suggested that the heat extraction expands the range of stable MILD combustion for oxygen-enriched conditions. Other researchers who addressed this problem are Wang et al. [19]. They investigated the numerical feasibility of LGC implementation in conditions of high heat extraction. It turned out that LGC cannot be sustained if the ratio of extracted heat to input energy of the fuel exceeds 57%. However, after introducing the so-called Internal Recirculation Device (IRD), LGC can be maintained in such conditions up to 88%. In their recent work, Xu et al. [26] investigated another way to offset the high heat extraction effects so that LGC can be maintained—hydrogen. According to their analysis, MILD combustion of hydrogen-enriched methane can be sustained even up to 91% of the heat extraction ratio if the substrates are pre-heated up to 1200 K.

The aforementioned works are a good indication of slowly increasing interest in transferring LGC technology to industrial small-scale boilers. Luan et al. [25] and Xu et al. [26] used a 0-deminsional WSR model which shed some light on the much needed theoretical and process-based aspects of LGC behaviour under high heat extraction. On the other hand, their analyses are limited to preliminary process-feasibility studies, as there are no geometrical nor material properties of the furnace involved. Xu et al. [24] in their previous work developed a 3D numerical model based on their lab-scale furnace and used it in the numerical exploration of high heat extraction impact on LGC. Further steps towards potential implementation of LGC in fire-tube boilers has been made by Wang et al. [19]. They proposed a solution that is potentially easy to implement as it consists of a solid insert introduced to the combustion chamber which separates the reaction zone from the "cold" walls. Results of their work are very promising and constitute a good starting point for further analyses. The idea presented in their work has been recently investigated by Mohammadzadeh Pormehr et al. [27]. They experimentally and numerically investigated a rectangular furnace equipped with a solid insert, called a deflector. The deflector had two arms on the burner side at an angle of 45°. During their numerical study, the angle and length of the arms were examined. According to their results, both parameters have an impact on the combustion conditions and products, i.e., arms' length up to 60 mm enhances recirculation by over 20%, whereas recirculation at a length past 60 mm decreases by almost 30%. Also, an arm angle of 45° provided the highest recirculation coefficient. It was also observed that the length of the arms exert some negative impacts on NO emission.

Since an IRD or deflector inserted into a combustion chamber are relatively easy to implement and their severe effects on low-gradient combustion conditions, stability, and products have been shown, they can be even more attractive for researchers and industry. For this reason, the authors dedicated this paper to investigate this issue even further. They used a model proposed by Wang et al. [19] and made a preliminary investigation into the potential application of IRDs in low-gradient combustion in conditions close to the real operation conditions of a fire-tube boiler. This was done by changing the fixed wall temperature (or fixed heat flux) boundary condition to a convective boundary condition with estimated boiling coefficient. The analysis is focused on a numerical investigation of pollutants emissions, radiative, convective, and conductive heat fluxes in both traditional and low-gradient combustion regimes. The analysis has been supplemented with the examination of one geometrical and one material parameter of the IRD: three different diameters and several thermal conductivity coefficients. This allowed the authors to assess and compare the thermal efficiency of low-gradient and traditional combustion regimes as well as assess the effect of the IRD's diameter and material on LGC stability and emissions, which is the main outcome of this work. Unfavorability towards LGC high heat extraction and lack of combustion substrates pre-heating are also addressed.

2. Construction and Operation Principle of Fire-Tube Boiler

Construction of fire-tube boilers (sometimes called flame-tube boilers [3]) depends mainly on the required power output, fuel, available space, or steam parameters. There are many variants offered by manufacturers, depending on orientation: horizontally oriented [28] or vertically oriented [2]; number of passes: single [28], two- [1,6] or three-pass [5,29]; or flame direction: forward [8] or reverse [14,30]. Two of them are presented in Figure 1: a so-called reverse flame (Figure 1a) and the most popular variant being a three-pass boiler with forward flame (Figure 1b). In both cases, a low-NO burner (1) supplies the flame tube (2) that is immersed in boiling water contained in a water shell (7). In the reverse flame, the flue gas is reversed inside the combustion chamber (which is larger than in other variants) and then directed to smoke tubes (4) via reverse chambers (3), an economizer (5), and finally to the environment (6). Steam is gathered in the upper part of the shell (7) beyond the water level (9), extracted through a valve (8) and, at the end, returned to the shell as a condensate. In the three-pass, the flue gas flows directly to the smoke tubes.

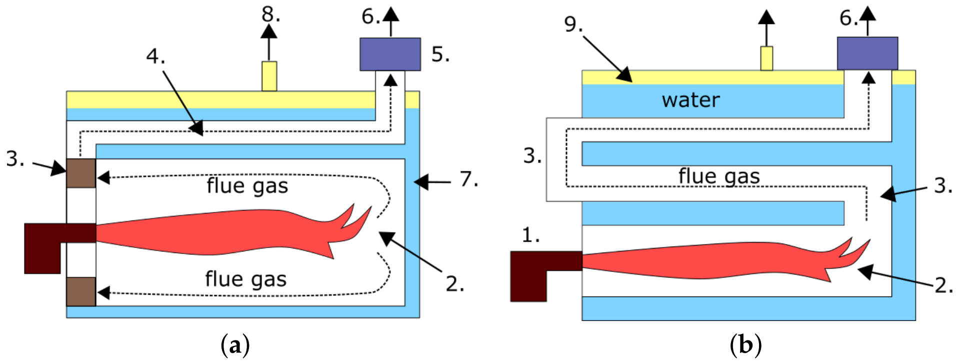

Figure 1. Schematic representation of two fire-tube variants: (**a**) reverse flame. (**b**) Three-pass boiler. 1—burner, 2—flame tube, 3—reverse chamber, 4—smoke tubes, 5—economizer, 6—exhaust to the environment, 7—water shell, 8—steam valve, 9—water level.

3. Numerical Analysis

3.1. Computational Domains and Numerical Meshes

Numerical analysis covers two stages: 1—model validation via data provided by Wang et al. [19] and their previous work [31]; 2—a numerical study including implementation of convective boundary condition (BC) instead of temperature BC and analysis of the IRD diameter's impact on the heat transfer and emissions of the species-of-interest.

In the first stage, two computational domains were recreated to be exactly the same as in [19,31]—one for traditional combustion (TC) and one for low-gradient combustion (LGC). They cover a 2-dimensional axisymmetric slice of a cylindrical furnace. Both domains are presented in Figure 2. All given dimensions from the works of Wang and Shu are preserved. The domains were created in Ansys DesignModeler.

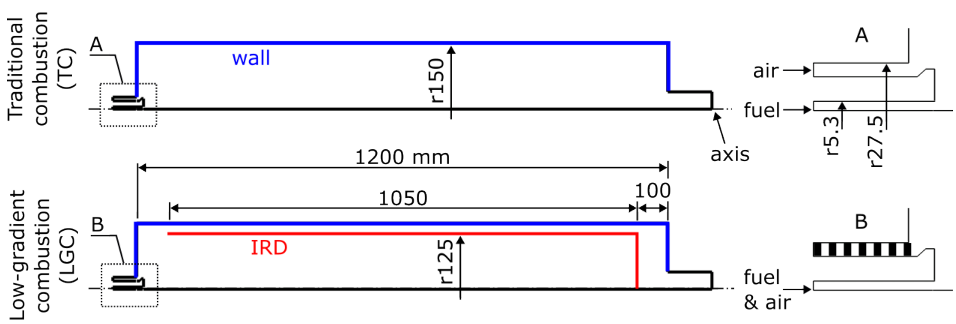

Figure 2. Computational domain and burner configuration: traditional combustion (TC)—non-premixed; low-gradient combustion (LGC)—premixed. IRD—Internal Recirculation Device. Detail A—TC burner configuration. Detail B—LGC burner configuration.

Accordingly, two numerical meshes shown in Figure 3 were prepared in such a way as to be possibly close to the originals from the work of Wang and Shu—one for traditional combustion (Figure 3a) and one for low-gradient combustion (Figure 3b). Both meshes are structured and consist of 61k and 65k quadrilateral elements, respectively. Ansys Mesher was used for meshing.

3.2. General Setup of the Numerical Model

Next, both numerical models were prepared and solved in Ansys Fluent 2021R1, both in a steady-state with the gravity turned on in parallel to X-axis (which corresponds with vertical orientation of the real furnace). General setup is the same as in Wang et al. [19], namely a standard k-ε model with standard wall functions was employed for turbulence modeling. An Eddy Dissipation Concept (EDC) model was used for turbulence–chemistry interaction along with a GRI-Mech 2.11 mechanism. Radiation was taken into account via Discrete Ordinates (DO) and Weighted-Sum-of-Gray-Gases (WSGGM) models. All model constants had default values, as any alterations were not mentioned in [19] nor in [31]. SIMPLE scheme was chosen for pressure–velocity coupling, Least Squares Cell-Based for gradient discretization, Second Order for pressure discretization, and Second Order Upwind for momentum, turbulence, energy, and discrete ordinates discretization, whereas Quick scheme was used for species.

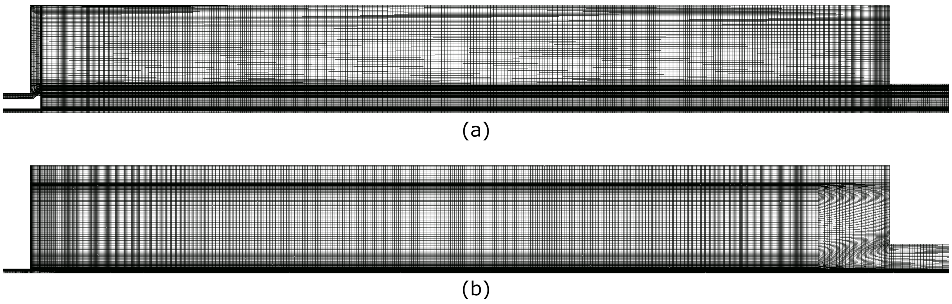

Figure 3. Numerical meshes: (**a**) traditional combustion—61k elements. (**b**) Low-gradient combustion—65k elements.

In the TC case, fuel and air were supplied separately via two nozzles (see Figure 2, detail A) at 290 K and at a normal pressure of 101,325 Pa, contrary to [19], where the furnace originally operated at a slightly elevated pressure (not specified). The fuel was composed of 89.2% CH_4, 7.8% C_2H_6, and 3% H_2 (all% in vol). Also, mass flow inlet boundary conditions were used (in contrast to velocity inlets in [19]) in this model for applying the substrates at 0.000384 kg/s and 0.007611937 kg/s of fuel and air, respectively. The change in inlet BC from velocity to mass enabled direct control of the flow rate regardless of operating pressure. Air flow rate was adjusted to maintain an equivalence ratio at 0.86.

In the LGC case, mass flow rates of the fuel and air were merged and supplied via the previous fuel nozzle (see Figure 2, detail B). Recalculated volumetric composition of the mixture is as follows: 7.1% CH_4, 0.6% C_2H_6, 0.2% H_2, 19.3% O_2, and 72.7% N_2. In both the TC and LGC cases, fuel stream and composition should provide power input at approx. 19.2 kW.

3.3. Validation—Reference Results

In the first step of validation, both TC and LGC cases were solved at a constant wall (blue line in Figure 1) temperature set to 1340 K, which, the author assumes, is close to the average experimental value from Shu et al. [31] (not specified explicitly). The computations were carried out until outlet average the temperature, chosen species fractions, and energy balance stabilized. Also, an energy balance inconsistency < 1% was an additional stop criterion.

The obtained temperature fields are presented in Figure 4, and, according to the expectations, in traditional combustion a flame front is clearly visible (red) and provides a much higher peak temperature than low-gradient combustion—2085 K and 1488 K, respectively. In LGC, the temperature distribution is much more uniform—zone > 1376 K takes approximately 3/4 of the available space.

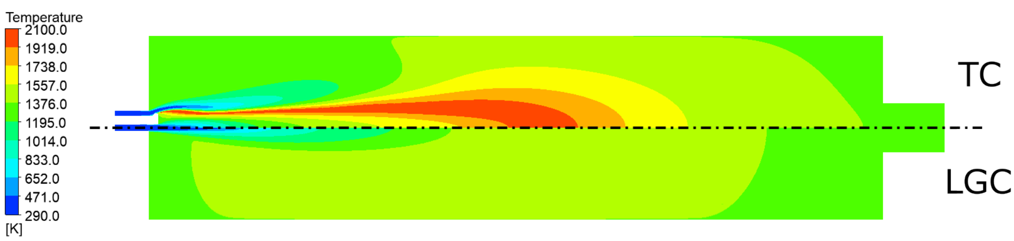

Figure 4. Temperature field of the reference TC and LGC cases. TC—traditional combustion; LGC—low-gradient combustion.

Predicted emissions of O_2, CO_2, CO, and NO in both combustion modes were also compared with experimental (EXP) and numerical (CFD) data provided by Shu et al. [31]. In Figure 5 results of the TC mode are presented. Clearly, due to similar yet different combustion conditions (i.e., wall temperature, operating pressure), the model used in this work shows some discrepancies for all the species. O_2, CO_2, and CO emissions are underpredicted by approx. 0.5%, 2%, and 10 ppm, respectively, whereas NO emission is overpredicted by about 30 ppm. However, a general trend is maintained: about 3% of oxygen, 9% CO_2, small amount of CO, and high NO emission.

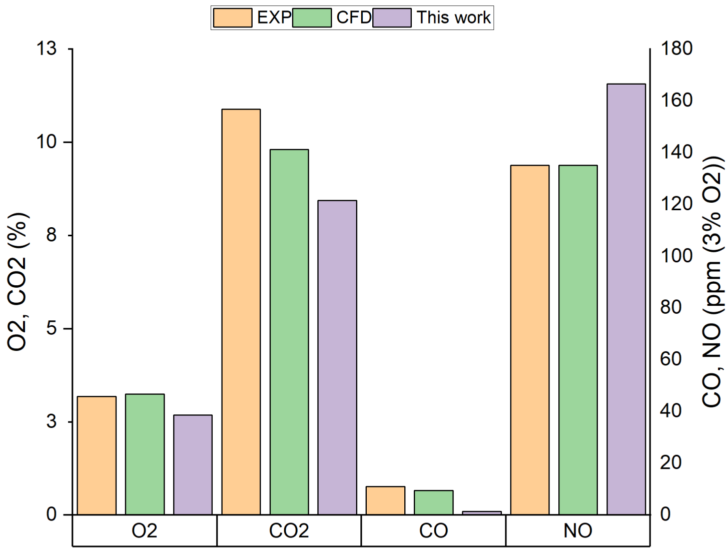

Figure 5. Emissions comparison of TC mode. EXP—experimental data, CFD—simulation data taken from [31]. Work-simulation data taken from this work.

The same comparison has been done for the LGC mode, results of which are shown in Figure 6. Predicted emissions of O_2, CO_2, CO, and NO manifest similar behavior as in TC—there is a slight underprediction in regards to the experimental values, but the quantitative trend remains reflected. Thus, it can be concluded that the model is properly set and can be used in further computations.

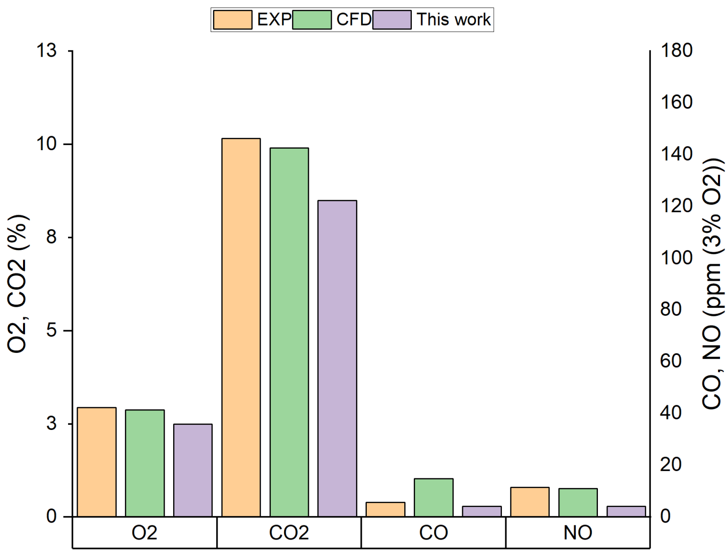

Figure 6. Emissions comparison of LGC mode. EXP—experimental data, CFD—simulation data taken from [31]. Work-simulation data taken from this work.

4. Results and Discussion

4.1. High Heat Extraction Conditions

So far, the model has been validated against experimental data provided by [31]. These data, however, were collected in laboratory conditions with the thermally insulated external wall of the furnace—hence, the estimated temperature of 1340 K and significantly limited heat losses. Fire-tube boilers work in opposite conditions, as the fire tube (combustion chamber) is not thermally insulated and, in addition to this, is immersed in a water tank filled with boiling water. The idea of this analysis is to numerically investigate, whether or not the LGC can be sustained in conditions similar to the operating conditions of the real boiler. To do so, the wall temperature BC has been changed to a convective BC (instead of artificially imposing a fixed temperature). As the fire-tube is immersed in slightly pressurized water (here assumed to be 20 bars as this is the typical operating pressure for this kind of device [5,9,10]) and the heat is transferred directly to the fluid, the water boils in direct vicinity of the fire-tube wall. Additionally, according to the boiling curve, nucleate boiling is desired [32]. Thus, Rosenhow's equation [32] has been employed for estimation of the nucleate heat flux (W/m^2) given in the following expression

$$\dot{q}_{nucleate} = \mu_l h_{fg} \left[\frac{(g(\rho_l - \rho_v))}{\sigma} \right]^{(1/2)} \left[\frac{c_{pl}(t_s - t_{sat})}{C_{sf} h_{fg} \mathrm{Pr}_l^n} \right]^3 \tag{1}$$

where μ_l—viscosity (liquid), kg/(m·s); h_{fg}—enthalpy of vaporization, J/kg; g—gravitational acceleration, m/s^2; ρ_l—density of the liquid, kg/m^3; ρ_v—density of vapor, kg/m^3; σ—surface tension of the liquid, N/m; c_{pl}—specific heat of the liquid, J/(kg·°C); t_s—Surface temperature, °C; t_{sat}—saturation temperature of the liquid, °C; C_{sf}—experimental constant depending on surface-liquid configuration; Pr_l—Prandtl number of the liquid; and n—experimental constant depending on the fluid.

Constants C_{sf} and n were provided by [32], and take the values of 0.013 and 1, respectively. Temperature t_{sat} results from the pressure and for 20 bars equals approx. 210 °C, whereas t_s had to be determined. Keeping in mind that the wall of the fire-tube is a rolled metal sheet (with small thermal resistance), the surface temperature was assumed to be 5 °C above the t_{sat}. This is a rough assumption, but will suffice for the sake of a preliminary character of these analyses. Additionally, a similar temperature (but as temperature BC) was assumed by Morelli et al. [1].

Next, the boiling heat transfer coefficient (W/(m^2·°C)) was determined with the use of an expression based on Newton's Law

$$h_{nucleate} = \frac{\dot{q}_{nucleate}}{t_s - t_{sat}} \tag{2}$$

Finally, $h_{nucleate}$ took the value of 23,658 W/(m^2·°C) and was applied in the convective boundary condition along with thermal conductivity of the wall 16 W/(m·°C), which is provided by Fluent's predefined material—steel. Wall thickness was set to 5 mm and free stream temperature set to 205 °C—both values are assumed.

In the next step, both TC and LGC were analyzed in Fluent under new conditions. Unsurprisingly, traditional combustion was sustained, whereas LGC did go extinct due to excessive cooling of the reaction zone, which eventually led to atrophy of the chemical reactions. The situation did not change even after changing the temperature of the fuel and air from 290 K to 1290 K, which correspond with recuperation. Recuperation is only theoretical, since the temperature of exhaust gases produced by a fire-tube boiler often does not exceed 150 °C. Temperature profiles of traditional combustion and low-gradient combustion (of the preheated substrates) are presented in Figure 7. The temperature of the flame in TC mode is noticeably lower (by approx. 400 °C) than in the previous conditions with fixed wall temperature (shown in Figure 4). In LGC mode (with preheated substrates) a slight temperature increase can be noticed. This, however, is a result of an influx in the hot substrates.

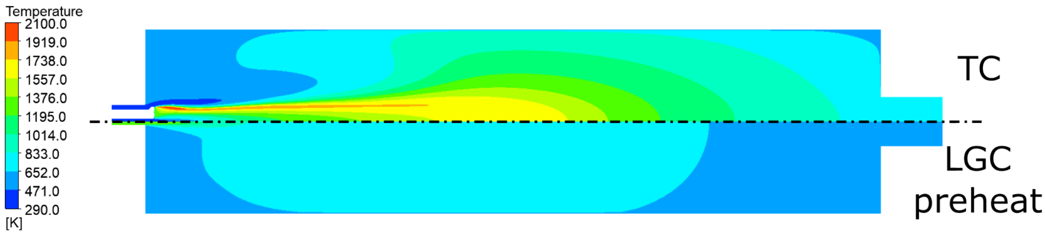

Figure 7. Temperature distribution during high heat extraction via external wall. TC—traditional combustion; LGC preheat—failed low-gradient combustion (no combustion) of substrates preheated up to 1290 K.

Predicted emissions of TC mode under both wall boundary conditions are gathered in Table 1. CO emission increased rapidly from 1.3 ppm to 48.5 ppm in the case of high heat extraction. The level of NO_2 was also elevated (23.7 ppm), whereas total emission of nitrogen oxides (NO_x) remained similar (162.5 and 166.1 ppm) in both conditions. Apparently, concentration of NO_2 should be tracked along with NO in further analyses.

Table 1. Predicted emissions of TC under fixed wall temperature T_{wall} and fixed boiling heat transfer coefficient $h_{nucleate}$.

Wall BC	O_2 %	CO_2 %	CO ppm	NO ppm	NO_2 ppm	NO_x * ppm
T_{wall}	2.7	8.4	1.3	162.1	0.4	162.5
$h_{nucleate}$	2.8	8.4	48.5	142.4	23.7	166.1

* Sum of NO and NO_2.

4.2. Impact of the IRD on Combustion and Emissions

A previous analysis showed that low-gradient combustion cannot be maintained in the fire-tube boiler conditions of high heat extraction. This fact may shed some light on why LGC technology is absent in contemporary industrial fire-tube boilers. However, a solution proposed by Wang et al. [19] can be a remedy to this issue, but its impact on heat and mass transfer requires a deeper understanding. It is called by Wang et al. an Internal Recirculation Device (IRD) and, basically, it is a cylindrical insert made of insulating material. IRD works as a screen that mediates heat transfer between the reaction zone and the walls and divides the combustion chamber into two zones, easily distinguishable in Figure 8. Zone 1 is located on the flame side where temperatures above 700 K prevails, while noticeable cooler zone 2 lays between the IRD and the external wall. In the figure, two cases are presented: one with thermal conductivity of the IRD k_{IRD} = 0.1 W/(m·K) and one with k_{IRD} = 0.9 W/(m·K). In all analyzed cases the thickness of the IRD was kept constant and amounted to 15 mm. Contrary to the LGC case without the IRD, in analyses with the IRD introduced, the reactions managed to occur within zone 1, despite the high heat extraction due to convective BC at the wall.

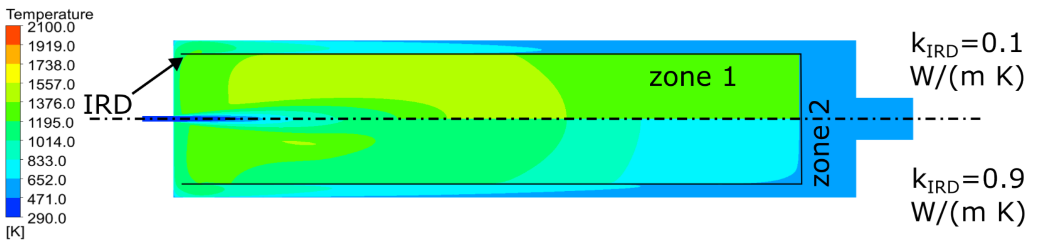

Figure 8. Temperature field in LGC with high heat extraction and IRD. k_{IRD}—thermal conductivity of the IRD.

Moreover, thermal conductivity of the IRD has a serious impact on the temperature in zone 1: peak temperature in the first case equals 1461 K, while in the second case (with higher k_{IRD}) it is equal to 1380 K. One should also notice that the actual reaction zone can be smaller than zone 1, as it shrinks towards the burner as thermal resistance of the IRD decreases. As a result, two sub-zones are created within zone 1: 1.a—reaction zone (near the burner) and 1.b—low-temperature zone (on the blinded side of the IRD).

Thermal resistance of the IRD also impacts NO_2 emissions. Namely, the higher the k_{IRD}, the higher the NO_2 concentration, which is presented in Figure 9a (red line). NO_2 emissions rise from ≈25 ppm to ≈65 ppm for k_{IRD}, ranging from 0.1 to 0.9 W/(m·K), respectively. On the other hand, NO emission stays at nearly negligible level (less than 5 ppm) in all cases. Apparently, the NO_2 mechanism is predominant and has to be taken into account while calculating total NO_x emissions. Additionally, above k_{IRD} = 0.9 W/(m·K), a consistent flame extinction was observed, which confirms observations made in Wang et al. [19]. It also implies the serious impact of the heat transfer conditions on the critical k_{IRD} value, which may be valuable knowledge for the design of IRDs. Namely, k_{IRD} should be possibly low due to flame oscillations and safety in maintaining combustion. k_{IRD} also should not be too low, as NO_2 emission can rise above the acceptable limit.

To this point, all the numerical analyses were carried out at a constant equivalence ratio of 0.86 (Baseline Case). To investigate more deeply the behavior of LGC with IRD in high heat extraction conditions, two additional values for the equivalence ratio were introduced: 0.80 (Case 2) and 0.74 (Case 3)Inlet Reynolds numbers (Re) and turbulence intensities were calculated for each equivalence ratio, which are summarized in Table 2.

Table 2. Reynolds number (Re) and turbulence intensity at the inlet.

Quantity name	Baseline Case	Case 2	Case 3
Equivalence ratio, -:	0.86	0.80	0.74
Re, -:	57,500	61,500	66,000
Turb. intensity, %:	4.1	4.0	4.0

The IRD was the same in all three cases (0.1 W/(m·K) and 15 mm of thickness), the results of which are presented in Figure 9b. According to the data, a decrease in the equivalence ratio results in an increase in NO_2 emission and decrease in the peak temperature. NO emissions consistently remained at negligible level in all three cases.

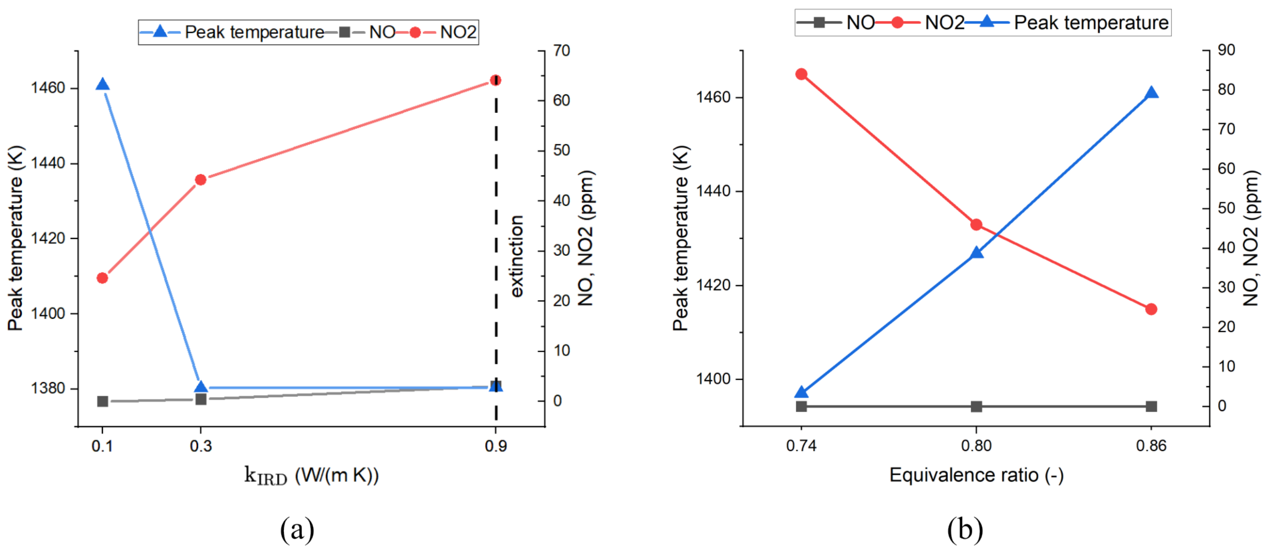

Figure 9. Peak temperature and NO, NO_2 emissions: (**a**) as a function of thermal conductivity of the IRD (k_{IRD}). (**b**) as a function of the equivalence ratio.

In the next step, the IRD diameter (d_{IRD}) and its impact on the combustion process were initially explored. It was changed from baseline value of 0.25 m to 0.275 m and to 0.225 m, which corresponds with a +10% increase and −10% decrease, respectively. The IRD thickness was, again, kept constant at 15 mm. In case of increased d_{IRD} to 0.275 m, flame extinction was numerically observed regardless of thermal conductivity of the IRD, which was in a range between 0.1–1 W/(m·K). On the other hand, the decreased diameter, d_{IRD} = 0.225 m, significantly shifted critical k_{IRD} towards higher values. Stable solutions were obtained up to k_{IRD} = 3.5 W/(m·K), whereas unconditional extinction was observed above k_{IRD} = 4.5 W/(m·K). In a range between 3.5–4.5 W/(m·K), some stability problems occurred, manifested by oscillations of the solution. Decrease in the under-relaxation factors did not solve the problem. Therefore, only results provided by the value of thermal conductivity up to 3.5 W/(m·K) are discussed in this section.

Emissions of CO, CO_2, and NO_x along with peak temperature at the outlet are presented in Figure 10 in the form of color maps. Thermal conductivity of the IRD k_{IRD} is presented on the abscissa axis, while the diameter of the IRD d_{IRD} is presented on the ordinate axis. The edge between the color map and white (empty) area denotes flame extinction or unconfirmed extinction. This edge, most probably, should take the form of a curve similar in shape to an ellipse if there were more IRD diameters investigated. Nevertheless, CO emissions in Figure 10a are arrange in sloped vertically oriented iso-lines, the values of which increase (steeply past 3 W/(m·K)) towards a higher k_{IRD}. Maximal CO emission (≈2620 ppm) corresponds with k_{IRD} = 3.5 W/(m·K), while minimal is located in a vast region between k_{IRD} = 0.1–0.9 W/(m·K). In case of CO_2 emissions (given in% (vol)) and presented in Figure 10b, the situation is opposite—minimal values (≈8.2%) can be observed for k_{IRD} = 3.5 W/(m·K), whereas maximal values are observed (≈8.5%) in the low k_{IRD} region and for an IRD diameter d_{IRD} = 0.25 m. In case of d_{IRD} = 0.225 m, CO_2 emissions are noticeably lower in a whole range of k_{IRD}.

Predicted numerically, emissions of NO_x are presented in Figure 10c. The iso-lines are also vertically oriented and only slightly sloped. It can be noticed that NO_x emissions increase in two directions: 1—higher k_{IRD} and 2—lower d_{IRD}. Therefore, the smaller the IRD diameter and the higher thermal conductivity of the IRD, the higher the expected NO_x emissions are. What is more, the increase is significant, as it raises from ≈10 ppm (which can be considered ultra-low NO_x [19,33]) to over 450 ppm. In other words, the IRD offers a significant NO_x emission reduction, but, in this particular case with a fixed wall thickness, only in a limited range of low thermal conductivities (below 0.5 W/(m·K)). Peak temperatures within the considered cases are presented in Figure 10d. As it can be noticed, the iso-lines arrange vertically and close to each other for values of k_{IRD} < 0.5 W/(m·K). They slightly deviate towards higher k_{IRD} values. The highest peak temperature (1524 K) was obtained in a case at the extreme of the considered range of the thermal conductivity and IRD diameter. Namely, at the lowest k_{IRD} and lowest d_{IRD}. Past k_{IRD} ≈ 0.7, the peak temperature becomes more uniform and slightly decreases as k_{IRD} increases, which manifests in some kind of a plateau (denoted as blue and light blue in color). The lowest peak temperatures were observed at the sloped edge of the color map, when the k_{IRD} was the highest, i.e., 0.9 and 3.5 W/(m·K). Based on all four color maps, one can determine an area (highlighted as a white dashed line) allowing for maintaining the lowest CO and NO_x emissions, and the highest CO_2 emission. As one can see, the area (in the explored range) takes the shape of a right-angled triangle with a (vertically oriented) base and hypotenuse converging at minimal d_{IRD} and minimal k_{IRD}. Orientation of the triangle suggests that possibly high d_{IRD} and low k_{IRD} are desirable for optimal operating conditions despite the overall operating range expanding with a lowering d_{IRD} and k_{IRD}.

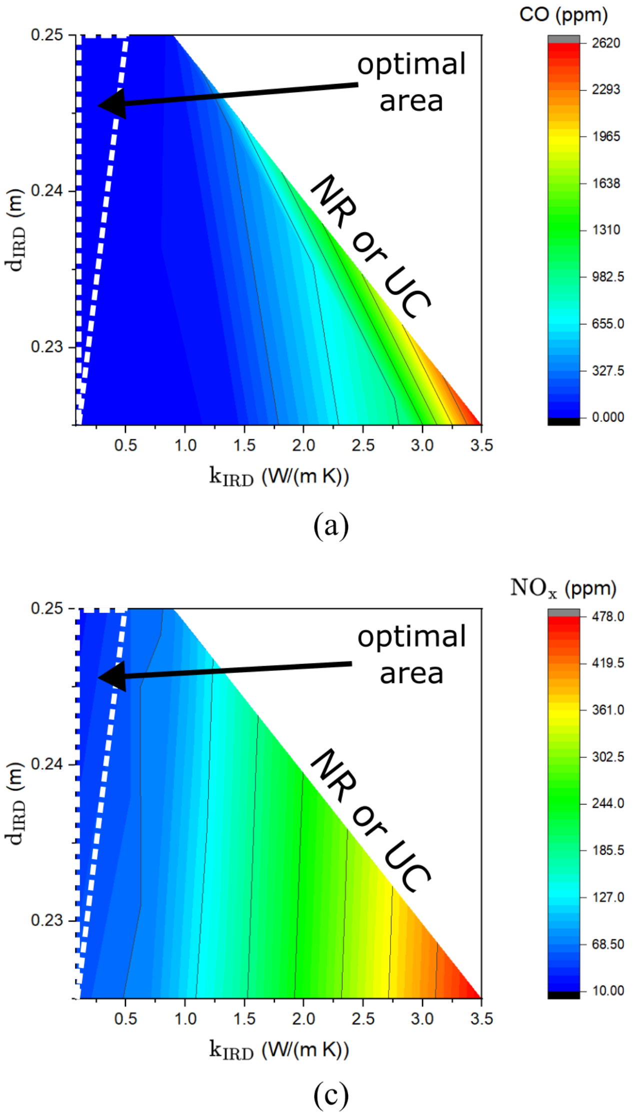

Figure 10. Color maps of four different quantities at the outlet in regards to diameter (d_{IRD}) and thermal conductivity (k_{IRD}) of the IRD: (**a**) CO emission. (**b**) CO_2 emission. (**c**) NO_x emission. (**d**) Peak temperature. White dashed line (optimal area)—IRD parameters allowing for the most optimal combustion. NR—no reactions; UC—unstable combustion.

It was mentioned previously (refer to Figure 9), that NO emission is negligibly small in comparison to NO_2 emission. The same applies to N_2O, which is highlighted in Figure 11a. In this figure, the NO_2 share in the total NO_x emission is presented in the form of bars. Except for two cases, the share of the NO_2 consistently exceeds 90% of the NO_x emission, whereas in TC mode this share amounts to only 14%. Stacked bars denoting separate NO and NO_2 emissions (given in ppm) are presented in Figure 11b. In the figure, it is clearly visible that overall the NO_x emission (NO + NO_2) is lower in the majority of LGC cases (except for LGC-0.225-3.5, LGC-0.225-2.9, and LGC-0.225-1.4) compared to the traditional combustion mode (TC). For the two highest k_{IRD} values (LGC-0.225-3.5 and LGC-0.225-2.9), the predicted NO_x are over two times the TC emission. For this reason, the IRD should be carefully designed, as it greatly impacts the emissions.

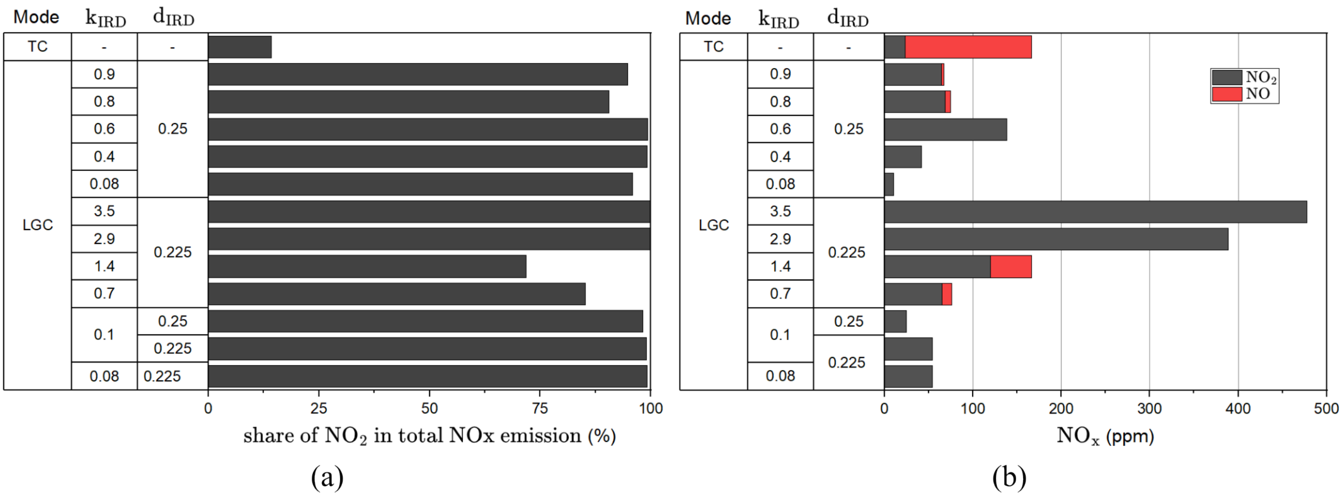

Figure 11. NO and NO_2. (**a**) Share of NO_2 in total NO_x emission. (**b**) Stacked emissions of NO and NO_2.

Apparently, introduction of the IRD radically changes the NO_x formation mechanism, which may be surprising, as in most other applications NO_2 exists as a transient species quickly destroyed in the post-flame zone. Hence, NO is generally the only significant NO_x species. However, situations in low-temperature combustion devices (<1150 K), such as gas turbines, are different and NO_2 can become dominant in NO_x emission [34–36]. In this case, the reaction zone with a relatively high temperature is limited by the IRD to the core of the combustion chamber, leaving its peripherals between the IRD and the external wall in a relatively low temperature (<1000 K). A relatively low equivalence ratio (high oxygen content)—in this case 0.86—also contributes to NO_2 formation, and the following reaction may take place [37]

$$NO + HO_2 \rightarrow NO_2 + OH \tag{3}$$

Reaction (3) proceeds rapidly at low temperatures, and reportedly, at temperatures of $\leq$750 °C still achieves equilibrium. According to this reaction, NO is consumed along with hydrogen peroxide and nitrogen dioxide is produced in the process. This may explain the low NO content and NO_2 domination.

To better visualize the impact of the IRD on the combustion conditions, a heat of reaction is presented in Figure 12 for three cases with different equivalence ratios Φ and different k_{IRD}. The heat of reaction is the released or absorbed energy as a result of the chemical reaction. In the first two cases with k_{IRD} = 0.1 W/(m · K), the shape of the heat of reaction contour is similar despite different equivalence ratios. In the case of Φ = 0.74, the reaction zone is slightly extended downstream when compared to Φ = 0.86 with k_{IRD} = 0.1. On the other hand, heat of reaction is compressed as it shrank significantly and moved upstream in the case of critical k_{IRD} = 0.9 W/(m · K). Since appropriate jet modeling may play an important role in reactive flows, same as it plays in the heat and mass transfer of non-reactive ones, it should be investigated more closely in future works, especially if some kind of a deflector is involved [38–43]. The majority of chemical reactions occur in transitional or fully developed regions, as in the potential core region the self-ignition temperature is not reached in this work due to the absence of substrates pre-heating.

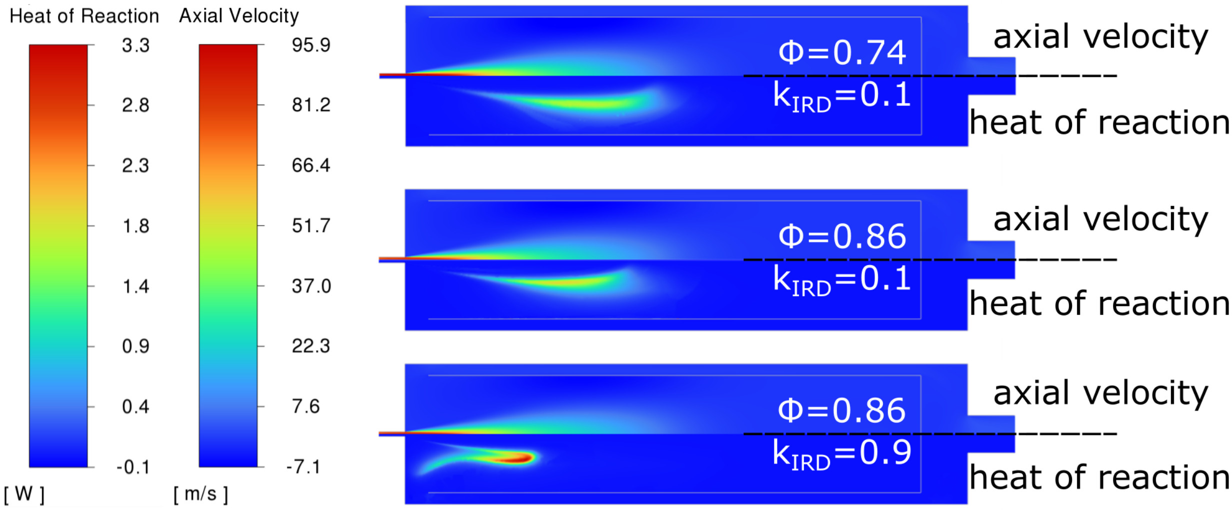

Figure 12. Axial velocity and heat of reaction: k_{IRD}—thermal conductivity of the IRD, $W/(m \cdot K)$, Φ—equivalence ratio, $-$.

The majority of chemical reactions occur in transitional or fully developed regions.

4.3. Heat Transfer with the IRD

Wang et al. [19] introduced a so-called heat extraction ratio defined as the ratio of the extracted heat transfer rate via the external wall to the enthalpy of the fuel

$$q_{ex} = \frac{\dot{Q}_{wall}}{\dot{Q}_{input}} \cdot 100\% \tag{4}$$

where q_{ex} stands for the heat extraction ratio,%, $\dot{Q}_{wall}$ denotes for the heat extracted from the combustion chamber through the external wall, W, and $\dot{Q}_{input}$ is the energy provided to the system, W. Hence, q_{extr} is defined in the same manner as renown energy efficiency η, and it can be called heat extraction efficiency. In their work, Wang et al. [19] were increasingly extracting heat from the furnace and observed that q_{extr} rises up to 88% and then remains constant. This study confirms their observation, which is illustrated in Figure 13 in the form of stacked columns. Each column represents separate case characterised by combustion mode (TC or LGC), boundary condition at the wall (fixed temperature 1340 K or convection $h_{nucleate}$), and diameter/thermal conductivity of the IRD d_{IRD}/k_{IRD}, respectively. Additionally, each column is divided into two parts denoted by two colors: red stands for radiative heat transfer mechanism, whereas dark-grey denotes the convective mechanism.

Looking at the first and second columns on the left-hand side (both concerning traditional combustion TC), one can notice that the change of the temperature BC (1340 K) to convection BC ($h_{nucleate}$) resulted in a significant increase in the q_{extr} from $\approx$45% to almost 80%. This was expected, as convective BC was meant to simulate high heat extraction from the furnace. In addition to this, the radiative mechanism in the first case is responsible for majority of the q_{extr} ($\approx$92% computed as $q_{radiative}/q_{extr}$), while in the second case (TC-h_{nucl}), only for $\approx$55%. This, again, was fully expected due to convective BC. Let us compare now the first and the third column—TC-1340-K with LGC-1340-K; in both cases, q_{extr} is almost the same. In the latter, however, the convective mechanism is noticeably larger, which results from increased recirculation within the reaction zone. In all the LGC-$h_{nucleate}$, regardless of d_{IRD} or k_{IRD}, heat extraction efficiency q_{extr} is, indeed, fixed at around 88%, with convection being responsible for $\approx$24% of the q_{extr} value.

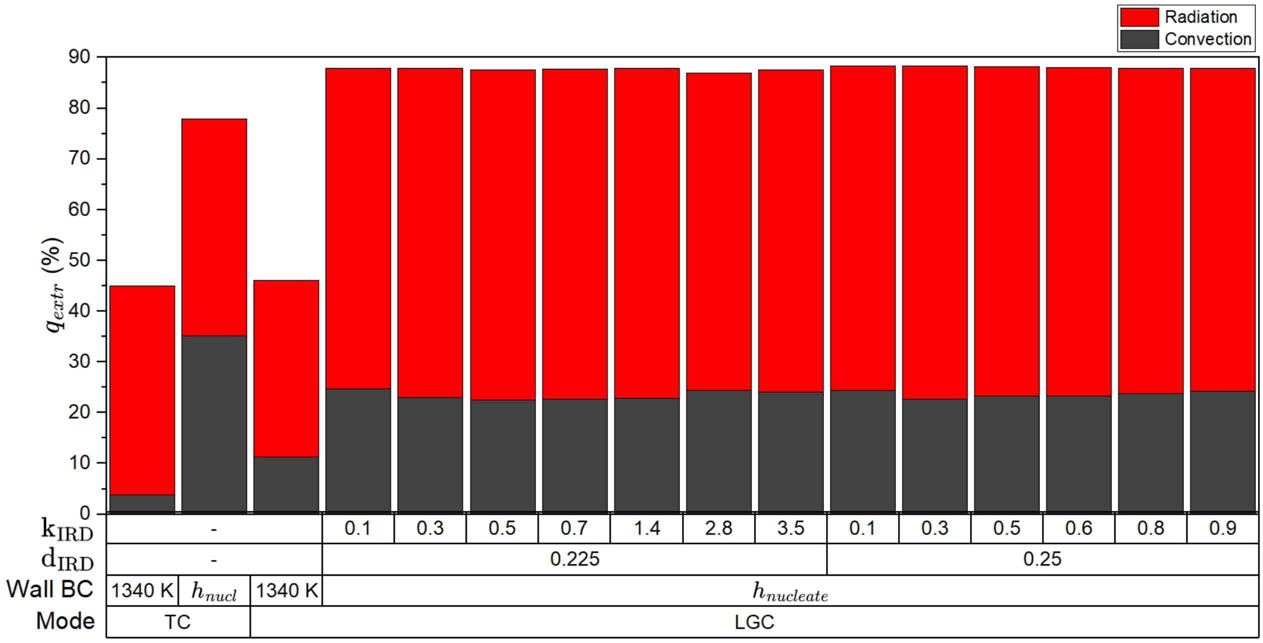

Figure 13. Heat transfer mechanism at the external wall of the furnace. TC—traditional combustion; LGC—low-gradient combustion; 1340 K—fixed wall temperature boundary condition; $h_{nucleate}$—convective boundary condition; d_{IRD} = 0.225 and d_{IRD} = 0.25—diameter of the IRD, m; k_{IRD}—thermal conductivity of the IRD, W/(m·K).

Based on the data collected in this work a conclusion can be drawn that high heat extraction from the combustion chamber impacts heat transfer and the chemical reaction mechanism. The difference lays in far-end effects: heat transfer via walls reaches its maximum at q_{extr} = 88% (in this work, this applies only to LGC mode), after which it stabilizes, while the substrates and combustion products are still influenced by temperature decrease. This, in turn, affects the chemical reaction pathways and, as a result, impacts the exhaust gas final composition (e.g., the significant CO and NO_x emission increase shown in Figure 10a,c). It should also be mentioned that, at the same power input, LGC heat extraction efficiency (in addition to being fixed at 88%) is approximately 10% higher than the TC-h_{nucl} case. This means that there is some potential for downscaling of the boiler using LGC technology with marginal negative effects on boiler efficiency or even with positive effects [13].

To verify the presumption above, seven heat fluxes along the external wall are presented in Figure 14. The solid red line denoted as TC (0/0) refers to traditional combustion without any IRD. Hence, (0/0) stands for k_{IRD} = 0 and d_{IRD} = 0, respectively. The short dash-dot and short dot black lines denoted as (0.1/0.25) and (0.9/0.25), respectively, stand for LGC with k_{IRD} = 0.1/d_{IRD} = 0.25 and k_{IRD} = 0.9/d_{IRD} = 0.25, respectively. Dashed and long dashed lines refer to the IRD diameter d_{IRD} = 0.225 at given thermal conductivities. The heat fluxes take negative values, but the (-) minus sign indicates only the direction of the heat transfer. So, negative values refer to the heat outflow, whereas positive values mean heat inflow.

At first glance, the most striking difference between TC heat flux and all LGC heat fluxes is its shape. The TC heat flux starts near zero (at this point it should be noted that the initial wall fragment that would be ahead of the IRD in LGC is not included in the figure), slowly rises, reaching a maximum value of ≈21,700 W/m^2 at ≈0.65 m, which corresponds well with the tip of the flame, as presented in Figure 4. Then, it decreases gradually until the end of the wall. The total heat flux in all LGC cases increases rapidly and reaches its maximum at ≈0.08 m (ahead of the IRD). Maximum heat flux across the cases varies significantly, from ≈30,000 W/m^2 to ≈53,000 W/m^2 in 3.5/0.225 and 0.1/0.25 series, respectively. Heat flux distributions in cases of the lowest thermal conductivity (k_{IRD} = 0.1), denoted by short dash-dot and short dash lines, are almost the same, regardless of the IRD diameter. The only difference between the two series is visible at the peak, where series 0.1/0.225 reaches ≈49,000 W/m^2 maximum value. Past the peak, the heat flux falls steeply up to 0.1 m and then continues to gradually decrease at a much lower rate beneath the TC (0/0) distribution. For higher values of k_{IRD} = <0.9, 3.5>, the peak is located at the same length, but is also much lower. A gradual heat flux decrease past 0.1 m changes slightly—it resembles a straight line in 0.9/0.25, while a common inflection point at 0.68 m is clearly visible in 1.4/0.225 and 3.5/0.225 distributions. Integration of the distributions corresponds well with total heat transfer rates given by Fluent. In other words, despite different shapes, integration at all LGC distributions gives practically the same result, which stands for ≈88% of the thermal power (19.2 kW, for the record). However, fixed convection at the external wall is not an ideal boundary condition (neither is fixed temperature nor fixed heat flux) and it can be useful to implement a conjugate heat transfer model, the benefits of which have been demonstrated by Xie et al. [44].

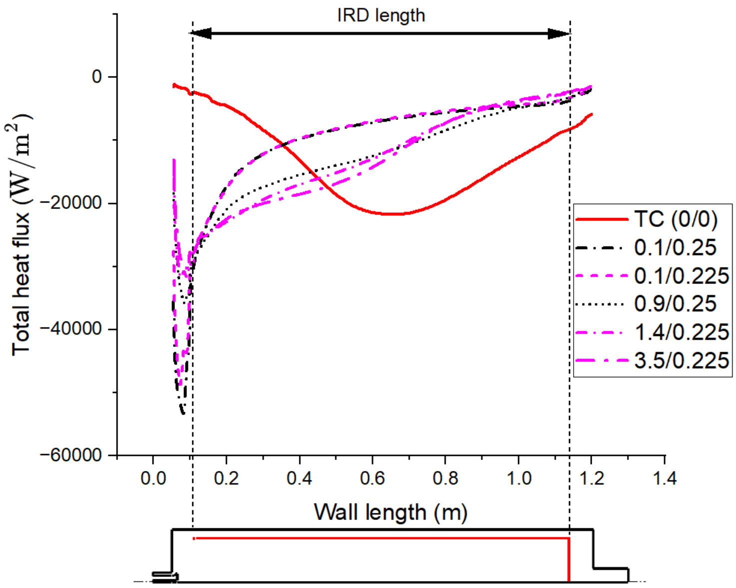

Figure 14. Total heat flux at the external wall of the combustion chamber.

5. Conclusions

To investigate the behavior of IRD-enhanced LGC technology in high heat extraction conditions characteristic for fire-tube boiler application, a thorough numerical analysis was performed and described in this study. A convective heat transfer coefficient has been estimated and applied as a boundary condition at the external wall of the chamber. Then, for different thermal conductivity coefficients of the IRD (k_{IRD}) and two different IRD diameters (d_{IRD}), the so-called heat extraction ratio (or heat extraction efficiency) q_{extr}, CO, and NO_x emissions, along with peak temperature and heat transfer mechanisms, were determined. Based on the results presented in Section 4, the following conclusions arise:

- Heat extraction efficiency q_{extr} is, indeed, capped at 88% after IRD introduction, regardless of IRD thermal conductivity k_{IRD} and diameter d_{IRD}. Also, critical k_{IRD} = 0.9 W/(m·K) at d_{IRD} = 0.25 m, beyond which combustion goes extinct, has been confirmed.
- Along with k_{IRD} increasing (past 1 W/(m·K)), the temperature decreases within the combustion chamber. As a result, NO_2 emission grows rapidly far above NO and N_2O emissions put together. The resulting total NO_x emission exceeds 150 ppm.
- IRD diameter d_{IRD} lowered from 0.25 to 0.225 (by 10%) shifts critical k_{IRD} towards higher values (from 0.9 W/(m·K) to at least 3.5 W/(m·K)). Consistent combustion extinction was observed even for low k_{IRD} = 0.1 after increase in the diameter from 0.25 to 0.275.

- Heat flux distribution at the external wall changes drastically after switching from TC to IRD-enhanced LGC. In TC mode, the distribution takes the shape of a bell curve (symmetrical to some extent), while in IRD-LGC, a steep gradient and extremum ahead of the IRD is noticeable, with a gradual decrease downstream. Additionally, LGC heat extraction efficiency (in addition to being fixed at 88%) is approximately 10% higher than TC heat extraction efficiency.
- Taking into account the serious impact of the IRD on CO and NO_x emissions, it should be very carefully designed in terms of material and its geometry to avoid excessive pollution and risk of flame extinction.

Author Contributions: Conceptualization, M.T. and R.B.; methodology, M.T.; software, M.T.; validation, M.T.; formal analysis, R.B.; investigation, M.T.; resources, M.T.; data curation, M.T.; writing—original draft preparation, M.T.; writing—review and editing, R.B.; visualization, M.T.; supervision, R.B. All authors have read and agreed to the published version of the manuscript.

Funding: This research received no external funding.

Data Availability Statement: Data available on request from the corresponding author.

Acknowledgments: The Authors were supported by the Ministry of Science and Higher Education, Poland, with the grant AGH UST no. 16.16.210.476 and by the NAWA Polish Returns no. 12.12.210.05020 (PPN/PPO/2019/1/00023/U/0001).

Conflicts of Interest: The authors declare no conflict of interest.

Abbreviations

The following abbreviations are used in this manuscript:

LGC	Low-Gradient Combustion
MILD	Moderate or Intense Low-oxygen Dilution
HiTAC	High-Temperature Air Combustion
HPAC	Highly Preheated Air Combustion
CFC	Colorless Distributed Combustion
FLOX	Flameless Oxidation
FC	Flameless Combustion
IRD	Internal Recirculation Device
BC	Boundary Condition
TC	Traditional Combustion (or conventional combustion)
EDC	Eddy Dissipation Concept
DO	Discrete Ordinates
WSGGM	Weighted-Sum-of-Gray-Gases Model
EXP	Experiment(al)
CFD	Computational Fluid Dynamics (or numerical)

References

1. Morelli, A.; Tognoli, M.; Ghidoni, A.; Najafi, B.; Rinaldi, F. Reduced FV modelling based on CFD database and experimental validation for the thermo-fluid dynamic simulation of flue gases in horizontal fire-tubes. *Int. J. Heat Mass Transf.* **2022**, *194*, 123033. [CrossRef]
2. Aguilar Vizcarra, D.; Esenarro, D.; Rodriguez, C. Three steps mixed (Fire tube–water tube) vertical boiler to optimize thermal performance. *Fluids* **2021**, *6*, 93. [CrossRef]
3. Kilic, G.; Sungur, B.; Topaloglu, B.; Ozcan, H. Experimental analysis on the performance and emissions of diesel/butanol/biodiesel blended fuels in a flame tube boiler. *Appl. Therm. Eng.* **2018**, *130*, 195–202. [CrossRef]
4. Gutiérrez Ortiz, F.J. Modeling of fire-tube boilers. *Appl. Therm. Eng.* **2011**, *31*, 3463–3478. [CrossRef]
5. Beyne, W.; Lecompte, S.; Ameel, B.; Daenens, D.; Van Belleghem, M.; De Paepe, M. Dynamic and steady state performance model of fire tube boilers with different turn boxes. *Appl. Therm. Eng.* **2019**, *149*, 1454–1462. [CrossRef]
6. Ferrarini, L.; Rastegarpour, S.; Landi, A. Experimental model validation and predictive control strategy for an industrial fire-tube boiler. *Therm. Sci. Eng. Prog.* **2022**, *36*, 101482. [CrossRef]
7. Habib, M.A.; Ben-Mansour, R.; Badr, H.M.; Ahmed, S.F.; Ghoniem, A.F. Computational fluid dynamic simulation of oxyfuel combustion in gas-fired water tube boilers. *Comput. Fluids* **2012**, *56*, 152–165. [CrossRef]

8. Batrakov, P.A. The Nitrogen Oxide Formation Studying at Natural Gas Combustion in Non-circular Profile Furnaces of Fire-tube Boilers. *Procedia Eng.*; **2016**, *152*, 144–150. [CrossRef]
9. Mansir, I.B.; Ben-Mansour, R.; Habib, M.A. Oxy-fuel combustion in a two-pass oxygen transport reactor for fire tube boiler application. *Appl. Energy* **2018**, *229*, 828–840. [CrossRef]
10. Habib, M.A.; Nemitallah, M.A. Design of an ion transport membrane reactor for application in fire tube boilers. *Energy* **2015**, *81*, 787–801. [CrossRef]
11. Zhao, T.; Chen, C.; Ye, H. CFD simulation of syngas combustion in a two-pass oxygen transport membrane reactor for fire tube boiler application. *Energies* **2021**, *14*, 7348. [CrossRef]
12. Sungur, B.; Topaloglu, B.; Ozcan, H. Effects of nanoparticle additives to diesel on the combustion performance and emissions of a flame tube boiler. *Energy* **2016**, *113*, 44–51. [CrossRef]
13. Tognoli, M.; Najafi, B.; Rinaldi, F. Dynamic modelling and optimal sizing of industrial fire-tube boilers for various demand profiles. *Appl. Therm. Eng.* **2018**, *132*, 341–351. [CrossRef]
14. Tognoli, M.; Najafi, B.; Marchesi, R.; Rinaldi, F. Dynamic modelling, experimental validation, and thermo-economic analysis of industrial fire-tube boilers with stagnation point reverse flow combustor. *Appl. Therm. Eng.* **2019**, *149*, 1394–1407. [CrossRef]
15. Buczyński, R.; Uryga-Bugajska, I.; Tokarski, M. Recent advances in low-gradient combustion modelling of hydrogen fuel blends. *Fuel* **2022**, *328*, 125265. [CrossRef]
16. Cavaliere, A.; De Joannon, M. Mild combustion. *Prog. Energy Combust. Sci.* **2004**, *30*, 329–366. [CrossRef]
17. Weber, R.; Mancini, M. On scaling and mathematical modelling of large scale industrial flames. *J. Energy Inst.* **2020**, *93*, 43–51. [CrossRef]
18. Wiinning, J.A.; Wiinning, J.G. Flameless Oxidation to Reduce Thermal No-Formation. *Prog. Energy Combust. Sci.* **1997**, *23*, 81–94. [CrossRef]
19. Wang, F.; Li, P.; Mi, J.; Shu, Z. A novel method to improve stability of MILD combustion in a highly heat-extracted furnace. *Fuel* **2021**, *292*, 120315. [CrossRef]
20. Sayadzadeh, M.E.; Samani, M.R.; Toghraie, D.; Emami, S.; Eftekhari, S.A. Numerical study on pollutant emissions characteristics and chemical and physical exergy analysis in Mild combustion. *Energy* **2023**, *278*, 128001. [CrossRef]
21. Tu, Y.; Su, K.; Liu, H.; Wang, Z.; Xie, Y.; Zheng, C.; Li, W. MILD combustion of natural gas using low preheating temperature air in an industrial furnace. *Fuel Process. Technol.* **2017**, *156*, 72–81. [CrossRef]
22. Galletti, C.; Parente, A.; Derudi, M.; Rota, R.; Tognotti, L. Numerical and experimental analysis of NO emissions from a lab-scale burner fed with hydrogen-enriched fuels and operating in MILD combustion. *Int. J. Hydrog. Energy* **2009**, *34*, 8339–8351. [CrossRef]
23. Mardani, A.; Karimi Motaalegh Mahalegi, H. Hydrogen enrichment of methane and syngas for MILD combustion. *Int. J. Hydrog. Energy* **2019**, *44*, 9423–9437. [CrossRef]
24. Xu, S.; Tu, Y.; Huang, P.; Luan, C.; Wang, Z.; Shi, B.; Liu, H.; Liu, Z. Effects of wall temperature on methane MILD combustion and heat transfer behaviors with non-preheated air. *Appl. Therm. Eng.* **2020**, *174*, 115282. [CrossRef].
25. Luan, C.; Xu, S.; Shi, B.; Tu, Y.; Liu, H.; Li, P.; Liu, Z. Re-Recognition of the MILD Combustion Regime by Initial Conditions of T_{in} and X_{O2} for Methane in a Nonadiabatic Well-Stirred Reactor. *Energy Fuels* **2020**, *34*, 2391–2404. [CrossRef]
26. Xu, S.; Tian, Z.; Tian, S.; Xi, L.; Tu, Y.; Liu, H. Sustainability of hydrogen-enriched methane MILD combustion over a wide range of hydrogen-blending ratios in a strongly heat-extracted well-stirred reactor. *Fuel* **2024**, *357*, 130035. [CrossRef]
27. Mohammadzadeh Pormehr, F.; Zabetian Targhi, M. Deflector design to improve internal gas recirculation in a MILD combustion laboratory furnace. *Fuel* **2024**, *360*, 130542. [CrossRef]
28. Andalia, W.; Pramadhony; Arita, S. Physical properties analysis of gases emission of blend biodiesel burning process in a fire tube boiler. *Int. J. Geomate* **2019**, *17*, 266–272. [CrossRef]
29. Kalyan, P.S.P.; Deshpande, A. CFD simulation of fuel/flue gas section of the fire tube steam boiler system. In Proceedings of the World Congress on Mechanical, Chemical, and Material Engineering, Virtual, 16–18 August 2020; Avestia Publishing: Orléans, ON, Canada, 2020; pp. 1–9. [CrossRef]
30. El-Mahallawy, F.M.; Mahdi Ali, E.; El-Asfouri, A.S.; Ibrahim, H.A. Combustion and heat transfer characteristics in boilers with asymmetrical reversed flow flame tube. *Exp. Therm. Fluid Sci.* **2003**, *27*, 417–430. [CrossRef]
31. Shu, Z.; Wang, F.; Dai, C.; Si, J.; Wang, B.; Mi, J. Characteristics of Nitric-Oxide Emissions from Traditional Flame and MILD Combustion Operating in a Laboratory-Scale Furnace. *J. Therm. Sci.* **2020**, *29*, 868–883. [CrossRef]
32. Çengel, Y.A. *Heat Transfer: A Practical Approach*, 3rd ed.; McGraw-Hill: Boston, MA, USA, 2007.
33. Arghode, V.K.; Gupta, A.K. Role of thermal intensity on operational characteristics of ultra-low emission colorless distributed combustion. *Appl. Energy* **2013**, *111*, 930–956. [CrossRef]
34. Smoot, L.D. *Fundamentals of Coal Combustion: For Clean and Efficient Use*; Elsevier: Amsterdam, The Netherlands, 1993; p. 755.
35. Szkarowski, A. *Spalanie Gazów—Teoria, Praktyka, Ekologia*, 2nd ed.; Wydawnictwo WNT: Warszawa, Poland, **2014**.
36. Glarborg, P.; Miller, J.A.; Ruscic, B.; Klippenstein, S.J. Modeling nitrogen chemistry in combustion. *Prog. Energy Combust. Sci.* **2018**, *67*, 31–68. [CrossRef]
37. Wilk, R.K. *Low-Emission Combustion*, 1st ed.; Wydawnictwo Politechniki Ślaskiej: Gliwice, Poland, 2002.
38. Rönnberg, K.; Duwig, C. Heat transfer and associated coherent structures of a single impinging jet from a round nozzle. *Int. J. Heat Mass Transf.* **2021**, *173*, 121197. [CrossRef]

39. Devahdhanush, V.S.; Mudawar, I. Critical Heat Flux of Confined Round Single Jet and Jet Array Impingement Boiling. *Int. J. Heat Mass Transf.* **2021**, *169*, 120857. [CrossRef]
40. Gurgul, S.; Fornalik-Wajs, E. On the Measure of the Heat Transfer Performance of RANS Turbulence Models in Single Round Jet Impingement. *Energies* **2023**, *16*, 7236. [CrossRef]
41. Angelino, M.; Di Venuta, I.; Boghi, A.; Petracci, I.; Gori, F. Further results on the mean mass transfer and fluid flow in a turbulent round jet. *Int. Commun. Heat Mass Transf.* **2023**, *141*, 106568. [CrossRef]
42. Di Venuta, I.; Boghi, A.; Angelino, M.; Petracci, I.; Gori, F. Numerical simulation and self-similarity of the mean mass transfer in turbulent round jets. *Int. Commun. Heat Mass Transf.* **2021**, *122*, 105146. [CrossRef]
43. Angioletti, M.; Nino, E.; Ruocco, G. CFD turbulent modelling of jet impingement and its validation by particle image velocimetry and mass transfer measurements. *Int. J. Therm. Sci.* **2005**, *44*, 349–356. [CrossRef]
44. Xie, M.; Tu, Y.; Peng, Q. Numerical study of NH3/CH4 MILD combustion with conjugate heat transfer model in a down-fired lab-scale furnace. *Appl. Energy Combust. Sci.* **2023**, *14*, 100144. [CrossRef]